



Simultaneous measurement of orthogonal terahertz fields via an emission multiplexing scheme

HUILIANG OU,¹  RAYKO IVANOV STANTCHEV,^{1,2,*}
XUEQUAN CHEN,^{3,4}  THIERRY BLU,⁵  MYKHAYLO SEMTSIV,⁶
WILLIAM TED MASSELINK,⁶ ARTURO HERNANDEZ SERRANO,¹
GONCALO COSTA,¹ JACOB YOUNG,¹ NISHTHA CHOPRA,¹
JAMES LLOYD-HUGHES,^{1,7} AND EMMA MACPHERSON^{1,8} 

¹Department of Physics, University of Warwick, Coventry CV4 7AL, United Kingdom

²Department of Physics, National Sun Yat-Sen University, Kaohsiung, Taiwan

³GBA Branch of Aerospace Information Research Institute, Chinese Academy of Sciences, Guangzhou 510700, China

⁴Guangdong Provincial Key Laboratory of Terahertz Quantum Electromagnetics, Guangzhou 510700, China

⁵Department of Electrical Engineering, Chinese University of Hong Kong, Hong Kong SAR, China

⁶Department of Physics, Humboldt University of Berlin, Berlin, Germany

⁷J.Lloyd-Hughes@warwick.ac.uk

⁸E.MacPherson@warwick.ac.uk

*Rayko.Stantchev@g-mail.nsysu.edu.tw

Abstract: We propose a polarization sensitive terahertz time-domain spectrometer that can record orthogonally polarized terahertz fields simultaneously, using fibre-coupled photoconductive antennas and a scheme that modulated the emitter's polarization. The *s* and *p* channels of the multi-pixel terahertz emitter were modulated at different frequencies, thereby allowing orthogonal waveforms to be demultiplexed from the recorded signal in post-processing. The performance of the multi-pixel emitter used in this multiplexing scheme was comparable to that of a commercial single-polarization H-dipole antenna. The approach allowed two orthogonally polarized terahertz pulses to be recorded with good signal to noise (>1000:1) within half a second. We verified the capability of the spectrometer by characterizing a birefringent crystal and by imaging a polarization-sensitive metamaterial. This work has significant potential to improve the speed of terahertz polarization sensitive applications, such as ellipsometry and imaging.

Published by Optica Publishing Group under the terms of the [Creative Commons Attribution 4.0 License](https://creativecommons.org/licenses/by/4.0/). Further distribution of this work must maintain attribution to the author(s) and the published article's title, journal citation, and DOI.

1. Introduction

Located in-between microwave and infrared radiation, terahertz (THz) waves loosely refer to electromagnetic radiation with frequency from 0.1 to 3 THz. Because of their relative long wavelengths and low photon energies, THz waves show significant potential in various applications such as imaging and tomography [1–3], material characterization and identification [4,5], astronomy [6] and wireless communication [7]. Terahertz time-domain spectroscopy (THz-TDS), featuring detection of the phase and amplitude of THz fields, serves an important platform for many scientific and industrial applications of THz light [8]. In addition to the phase and the amplitude, the polarization state of a THz field is important for material characterization, as it can provide even more information. For example, ellipsometry is well known for its high accuracy in obtaining the dielectric properties of samples by sensing the full polarization state of

electromagnetic waves [9,10]. Furthermore, vibrational circular dichroism spectroscopy (VCD) is carried out widely in biomolecular studies by determining the difference of the absorption between left-handed and right-handed polarized light, revealing the stereochemical structure of chiral molecules [11]. However, the above spectroscopies have rarely been employed in the THz range, mainly due to the challenge in precise manipulation and detection of polarization states at these frequencies. To date, the majority of THz-TDS systems rely on linearly polarized emitters and detectors and do not distinguish different polarization components. As a result, to fully measure the polarization states with conventional THz-TDS, multiple measurements have to be conducted separately and sequentially by mechanically rotating a polarizer (or a THz antenna or a detection crystal): such a procedure is time-consuming and subject to alignment errors and systematic error between different measurements. For example, laser pulse shifts caused by temperature variations in fibre-based THz-TDS can generate a phase error between two subsequent measurements, and the phase error has a significant influence in the reflection geometry and at high frequencies [12].

Several groups have attempted to modify conventional THz-TDS to perform polarization sensitive THz-TDS (PS THz-TDS) so that orthogonal polarization states are sensed simultaneously, or sequentially in rapid succession. In 1997, an early demonstration of PS THz-TDS utilized two independent photoconductive antennas (PCAs) to detect the orthogonal polarization components split by a free-standing wire grid polarizer using two detectors [13]. This apparatus was used to measure the THz Hall effect, and it halved the measurement time because one delay-line scan recorded both polarization components. Later in 2005, the same principle was applied to an electro-optic sampling setup with a (111) ZnTe detection crystal, offering equal sensitivity of both electric field components [14], although this required two pairs of balanced photodiodes. This is a disadvantage as it adds to the system complexity; further, electro-optic sampling is harder than a PCA to integrate into a compact, fibre-coupled detection unit. Nevertheless, the polarization sensitive imaging showed clear contrast features, demonstrating the method's usefulness [12].

In the same year, a rather elegant approach of using a multi-channel photoconductive antenna (MPCA) as a detector to sense the orthogonal polarization states was proposed by Castro-Camus *et al.* [15]. The photocurrent was restricted to either a horizontal or a vertical flow by two orthogonally aligned microscale channels formed by three electrodes, and thus two components of the incident waves were detected separately at the same time. From then on, different geometry designs of MPCA detectors were investigated, such as the triangle-gap design [16] and dual-bow-tie-shaped antennas [17]. However, cross-talk between the two detection channels can still be problematic in MPCA detectors if there is a large leakage current between the two channels, *i.e.* charge carriers will flow to the vertical detector channel even if you have a horizontal-only THz field. Last decade, new variants of the electro-optic (EO) sampling scheme were first proposed for rapid polarization resolved THz-TDS by quickly spinning the EO crystal [18], or by modulating the polarization of the laser probe beam using a photoelastic modulator (PEM) [19], or by analysing the polarizations state of the near-IR probe beam using an electro-optics modulator (EOM) [20]. The spinning EO method does not suffer from the long-term amplitude fluctuation of the THz waves, and the PEM and EOM methods avoid errors introduced by mechanical rotation of a polarizer. Later on, the spinning EO idea was applied to determine the polarization precision and calibration [21], and the EOM idea was applied to construct non-mechanical moving PS THz-TDS [22]. While these techniques are useful in EO sampling they are not applicable to THz detection via fibre-coupled PCA. Recently, Peng *et al.* [23] reported a cross-nanowire MPCA with high selectivity between orthogonal THz electric fields, and hence capable of recovering full polarization states without cross-talk, but with low signal to noise ratios and a challenging manufacturing process (stacking nanowires on top of each other in orthogonal orientations without touching).

In contrast to the above free-space approaches, fiber-based THz spectrometers are more compact, and allow straightforward changes to the incident angle of the THz beam without misalignment, which is essential for ellipsometry. To this end, rather than using a MPCA as a detector to record two components of a THz field, we report a system using a fiber-coupled MPCA as an emitter to generate two independent orthogonally-polarized THz fields, and a conventional H-dipole structure PCA as a detector to measure both fields. The orthogonally-polarized THz fields were generated using orthogonal THz pixels, biased by two sine waves at different frequencies, thereby allowing the separation of the two THz polarizations due to the orthogonality of the sine waves. In other words, we frequency-multiplex our emitted orthogonal polarization signals and demultiplex in post-processing. The complete fiber-based THz spectrometer is capable of measuring the full polarization states: in this article we detail the concept and performance of this new approach, which more than halves the data acquisition time by recording the orthogonal fields simultaneously and not needing to mechanically rotate a wire-grid polarizer. The concept and methods are described in Section 2, and validated in Section 3 where we highlight the low cross-talk and good polarization sensitivity of our method. Furthermore, we demonstrate the potential of this technique by characterizing a birefringent crystal (sapphire, Section 3.3) and taking polarization sensitive images of an anisotropic THz metamaterial (Section 3.4).

2. Method

2.1. PS THz-TDS

Figure 1 shows a schematic of our fibre-coupled PS THz-TDS concept. The system was composed of a femtosecond fiber laser, a mechanical optical delay unit (ODU), a THz source and detector, a data acquisition (DAQ) device and a computer. The femtosecond laser, ODU and THz detector were from MENLO System's Tera K15 kit. The THz source was a MPCA emitter made on InGaAs (detailed in Section 2.2). The THz detector was a commercial H-shaped stripline single-channel PCA. The THz source emitted horizontally (vertically) polarized THz pulses, shown in blue (red) in Fig. 1. The polarization sensitive H-shaped detector was placed at 45° to the horizontal, and produces an equal photocurrent for H or V emission if both channels have the same emission strength. A DAQ card was used to, on one hand, bias the two channels of the MPCA emitter with orthogonal waveforms, and also to record the voltage signal from the THz detector. The computer controlled the whole system and performed data post-processing (for details see Section 2.3). The emitter was encapsulated in a compact lens tube with a fibre collimator provided for fine laser alignment. The free-space THz beam was collected and focused by 2 pairs of TPX lenses in a standard transmission geometry spectrometer.

A laser pulse of 90 fs duration, 1550 nm central wavelength and 80 MHz repetition rate was split into two beams: the pump beam and the detection (gate) beam. The pump beam illuminated all four pixels of the THz source, and photoexcited free carriers, which were accelerated by the bias voltage and resulted in a photocurrent between the electrodes. The photocurrent dissipated rapidly because of the picosecond carrier lifetime of the InGaAs epilayer. Since the source was comprised of pixels with orthogonally-aligned electrodes, the photocurrent had both horizontal and vertical components. These rapidly-varying transient photocurrents thus emitted electromagnetic waves in the THz range with both horizontal and vertical polarization due to the structure of the electrodes.

To sample the two THz fields in the time domain, the detector was oriented at 45° to the horizontal, such that it recorded a voltage from either horizontally- or vertically-polarized THz beams. The arrival time of the detection beam was delayed by a rapid mechanical stage moving continuously across a 60ps scan range, and acquired at a 2.75 Hz frequency. The THz photocurrent in the detector was amplified, converted to a voltage by a trans-impedance amplifier, and recorded by the DAQ device.

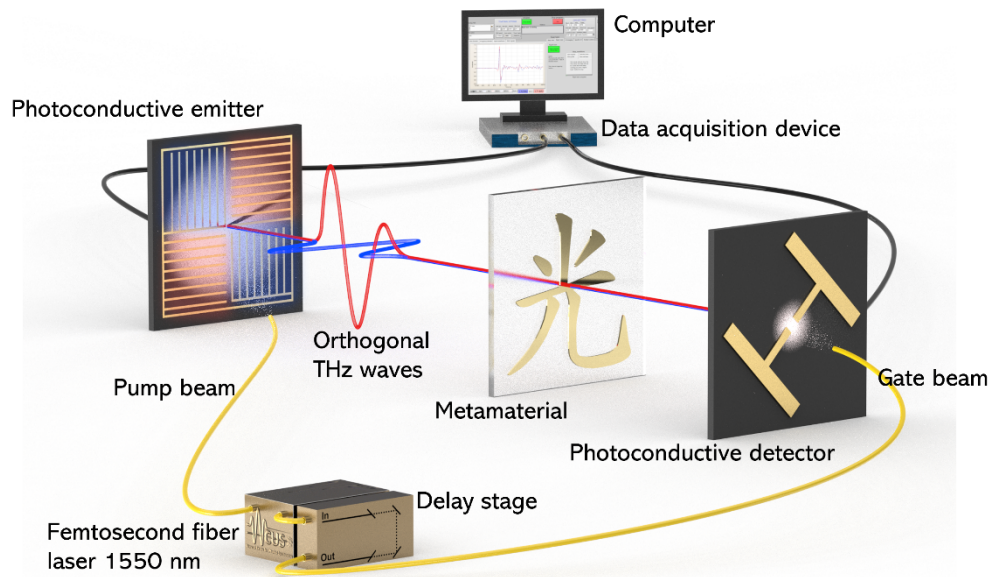


Fig. 1. Experimental illustration of the concept. From left to right, a multi-contact emitter is photoexcited by femtosecond laser (yellow cable) and each channel is modulated by two sine waves at different frequencies: $\sin \omega t$ for horizontal and $\cos 2\omega t$ for vertical and thus generating two orthogonal THz fields at ω and 2ω . After interacting with a sample, the orthogonal THz fields are recorded by a PCA detector placed at 45° to the THz fields, which is driven by the detection gate laser beam after passing through a delay stage. The separation of the two fields is performed by demultiplexing via computer post-processing. Note, many optical components such as lenses have been left out for visual clarity.

2.2. Interdigitated multi-contact photoconductive antenna

The interdigitated THz emitter had a repeated M-S-M-S (metal-semiconductor) configuration where two adjacent metallic microstrips serve as anode and cathode [24]. Compared to the conventional H-dipole structure, the adoption of an interdigitated shape introduces added benefits [25]. First, periodic microstrips increase the emissive area of semiconductor and thus overcome the saturation limits of a conventional PCA where the pump beam is focused to a small spot size. Second, a larger initial diameter for the THz beam leads to smaller beam divergence, so a hemispherical lens is not needed to collimate the THz beam. In addition, compared to the high voltage needed for a commercial H-dipole structure emitter (typically 100 V), the smaller gap between two metal strips allows the emitter to be driven by low voltages (less than 10 V), which is compatible with most signal generators and multi-purpose DAQ cards. Most importantly, a conventional two-contact PCA emits a substantial cross-polarized component, corresponding to a few percent of the main component [26,27]. In comparison, an interdigitated emitter acts as a wire-grid polarizer, so it emits almost pure linearly polarized light: for example a high polarization purity (ellipticity around 1°) in the bandwidth from 0.2 to 3 THz [28,29]. Further, it allows the construction of two nearby emitters that emit either vertically or horizontally polarized THz light with minimal cross-talk.

Figure 2 shows the microscope images of the interdigitated MPCA. We used conventional UV lithography and electron beam metal deposition to fabricate devices with the same geometry as previously reported [28], but using a short lifetime Rh-doped InGaAs epitaxial layer on an InP substrate [30] as the active semiconductor. InGaAs has a bandgap matching our excitation wavelength of 1550 nm, while Rh-doping created a material with a short (around 1ps)

recombination time [30]. The total emissive area was $300\ \mu\text{m} \times 300\ \mu\text{m}$, containing four pixels, each arranged orthogonally to its neighbor, as shown in Fig. 2(a). The vertical-emitting pixels are denoted V while the horizontal pixels are marked H. Figure 2(b) shows the cross-section view of part of one pixel to elucidate the structure of the active region. The gold layers were 300 nm thick, while the Al_2O_3 layer was 200 nm. The bottom gold layer served as the interdigitated electrodes to inject charges into the InGaAs. The Al_2O_3 layer acted as a dielectric spacer to separate the top and the bottom gold layer. The top gold layer served as a shadow mask to prevent destructive interference of the generated THz radiation in the far-field. Figure 2(c) shows an atomic force microscopy scan that confirms the deposited height and low surface roughness of the metal.

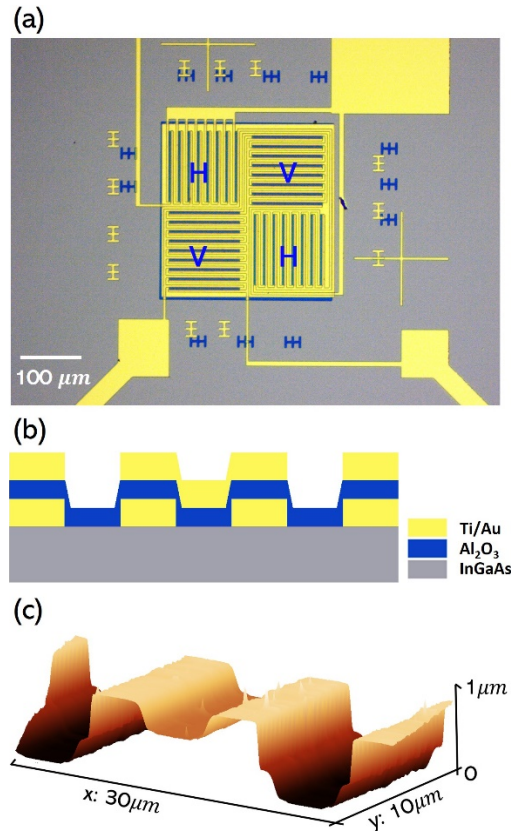


Fig. 2. Interdigitated MPCA. (a) Top view of the emitter from an optical microscope. The vertically and horizontally aligned electrodes are denoted as H and V. (b) Cross-section view of the emitter along 4 metallic microstrips. From bottom to top: InGaAs semiconductor (active material), Au interdigitated electrodes, Al_2O_3 dielectric spacer layer and Au shadow mask. (c) AFM scan of the cross section in (b). The measured height profile agrees well with the designed values.

2.3. Demultiplexing scheme

We now describe the demultiplexing procedure, applied during data acquisition, in more detail. In general, multiplexing allows separate signals to be sent over a shared medium without interference, so that a receiver can obtain the information from each individual channel. In our case we have two emitter channels (H and V), which are detected by a receiver that measures the sum of these two components. The simplest multiplexing scheme is to turn on each channel individually at

different times, in a technique called time-division multiplexing. However, this is inefficient: with our two-channel case, channels would be turned on for half the time. Alternatively, in frequency-division multiplexing the emitter channels are turned on continuously but at different frequencies, resulting in about twice the signal-to-noise ratio.

The principle of our demultiplexing scheme, based on frequency-division multiplexing, is as follows. The photocurrent signal measured by the PCA at a particular time delay t' between the THz pulse and the detection pulse, can be written as $I(t') \propto H(t') \sin(\omega t) + V(t') \cos(2\omega t)$, where $H(t')$ and $V(t')$ are the electric field amplitudes of the horizontal and vertical THz pulses, and $\sin(\omega t)$ and $\cos(2\omega t)$ describe the voltage waveforms biasing the emitter channels (the carrier waveforms) as a function of modulation time t . Multiplying $I(t')$ by $\sin(\omega t)$ or by $\cos(2\omega t)$ and then integrating over t readily allows $H(t')$ or $V(t')$ to be found by using the orthogonality of sine-waves.

Note that to integrate this approach with a rapid-scanning ODU, such that the recorded signal accurately reproduces the temporal shape of the THz pulse, the H and V signals must sample a narrow range of time delays t' shorter than the THz pulse duration. This requires a sufficiently fast sampling rate compared to the delay unit's scan speed, such that the demodulated signal is averaged over a small range of t' (say 200fs). Here, with an ODU scan rate of ~ 165 ps/s (a 60ps scan window, at 2.75 Hz), the optical delay t' changes by only ~ 17 fs during one modulation period ($100\mu\text{s}$ for $\omega/2\pi = 10$ kHz). We averaged over 10 modulation periods, corresponding to ~ 170 fs, and checked that the THz pulse shape obtained was the same as that obtained in step scan mode. More details are referred to [Supplement 1](#), Fig. S1-S3.

Note that sine and cosine were chosen as they are orthogonal functions (sine is an odd function; cosine is even), hence have zero overlap integral and minimum cross-talk. In terms of the orthogonality of these basis functions it is not essential that the modulation frequencies differ by a factor of 2, but some degree of separation in frequency space is useful so that the spectra can be effectively filtered by the band-pass filter. Further, since DAQ cards have a defined sampling interval, it is desirable for the periods of the modulation signals to be integer multiples of the sampling interval to avoid aliasing effects that might detrimentally alter the signal-to-noise and/or cross-talk.

3. Results

3.1. THz waveforms and spectra

With our interdigitated MPCA, orthogonally-polarized THz pulses were produced, denoted H (horizontal) and V (vertical), respectively. As discussed in Section 2.3, by modulating the two channels simultaneously, the H- and V- polarized THz pulses were obtained simultaneously with one delay-line scan. To demonstrate the efficacy of our demultiplexing scheme in separating the H- and V-polarized THz, we first assessed whether there was any cross-talk via the following method. We modulated each channel separately and checked for unwanted signal in the opposite channel after demultiplexing the signal. Specifically, in the first delay-line scan, we biased H with a $\sin(\omega t)$ waveform, while V was set to zero DC voltage, and then demodulated the total fields at frequencies ω and 2ω , resulting in the data shown in Fig. 3(a) and (b). Alternatively, in a second delay-line scan, we biased H with zero DC voltage and V with a $\cos(2\omega t)$ waveform: the ω and 2ω components of the demultiplexed signals are shown in Fig. 3(d) and (e). The background noise reported in Fig. 3(c) and (f) were measured with the detection beam on but with the MPCA off.

In Fig. 3(a) the H-polarized THz pulse can be seen, as obtained with H pixels biased at ω and the photocurrent demodulated at ω , while in Fig. 3(b) the demodulated signal at 2ω was comparable to the background noise, shown in Fig. 3(c). Therefore there was no substantial cross-talk when H was active and modulated at ω . Similarly, in the second delay-line scan, the V channel was obtained after demodulation at 2ω in Fig. 3(e), and Fig. 3(d) was similar to the noise

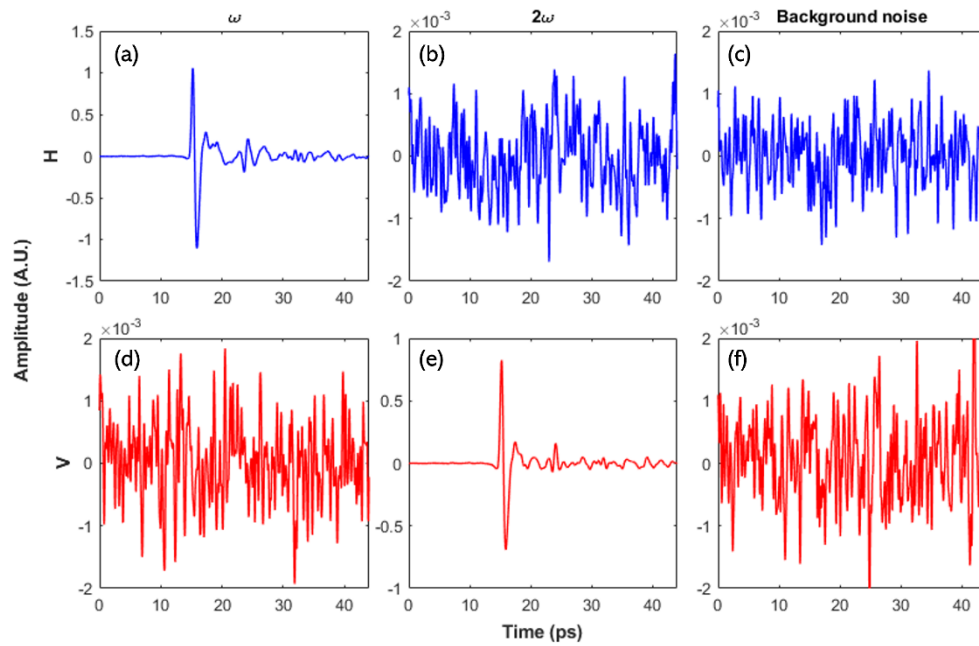


Fig. 3. Validation of the demultiplexing scheme. (a) and (b) show the demodulated photocurrents $H(t')$ and $V(t')$ with the H channel of the MPCA modulated at $\sin(\omega t)$ and the V channel grounded, while (c) shows the noise obtained with the MPCA off. (d)-(f) are similar to (a)-(c), but for a biasing scheme with V modulated at $\cos(2\omega t)$ and H grounded. Note the different y-axis scales for each plot.

of Fig. 3(f). Thus we concluded that there was no measurable cross-talk when obtaining the H and V polarized fields at ω and 2ω . No substantial difference for the H or V signal or cross-talk was evident in the frequency domain spectra, either when both channels were on separately or simultaneously (Supplement 1).

By applying the demultiplexing scheme, we obtained the orthogonal THz pulses shown by the blue and red lines in Fig. 4(a), shown offset vertically for clarity. To demonstrate the performance of the interdigitated MPCA, we compared the THz pulse with that of a commercial single-channel THz transmitter (Tera15-SL25-FC from Menlo Systems) by interchanging the emitters, and keeping all other parameters the same (*e.g.* excitation and detection laser power, applied bias voltage, identical optics and electronics). From Fig. 4 we can see that the MPCA had comparable performance to the commercial antenna. The signal-to-noise (SNR) of the MPCA channels, defined as the peak of the pulse divided by the standard deviation of the noise with the THz beam blocked, were 1075 and 1175, compared to 3785 for the commercial antenna. The higher SNR for the commercial antenna may be a result of it having a lower noise (for example because of a lower dark current) or smaller divergence angle (it had an integrated silicon lens), and our emitter split the power across two channels as opposed to one. The pulse duration of the MPCA is notably shorter than that of the commercial emitter (Fig. 4(a)), indicating that the MPCA had higher THz spectral bandwidth. As observed in Fig. 4(b), the MPCA spectral power was -30 dB at 2THz, while for the commercial emitter it reached -30 dB at 1.6THz. The greater spectral bandwidth could result from the photoconductor having a shorter carrier lifetime [31]; it could also arise from the increased loss at higher frequencies in the silicon lens used in the commercial emitter (no lens was used in the MPCA approach). The spectral amplitude of H and V channels of the MPCA were similar, with small differences assigned to either a non-uniform laser illumination

of the emission pixels, or a small difference in bias voltage. Also evident in Fig. 4(b) are the influence of absorption lines from water vapor absorption at 1.1 and 1.7 THz after time-domain windowing.

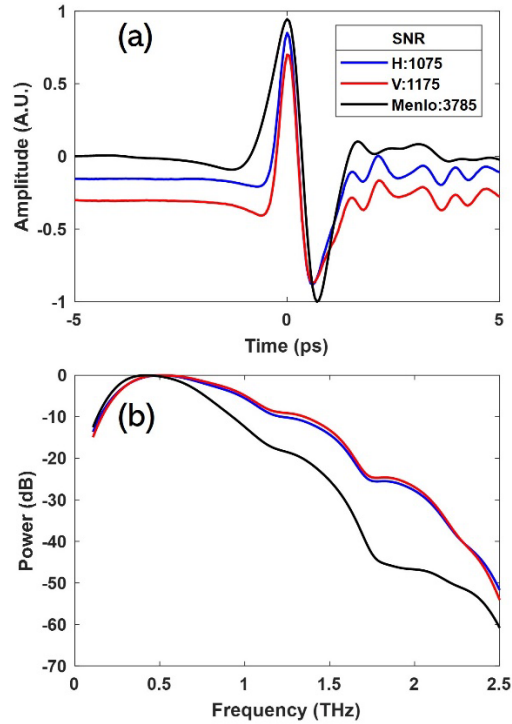


Fig. 4. Comparison between interdigitated MPCA and a commercial emitter. (a) THz time domain pulses from H, V and Menlo emitter. (b) THz frequency spectra from H, V and Menlo emitter, with gaussian filtering windows applied.

3.2. Polarization sensitivity

The polarization response of the system was examined by inserting a rotatable wire-grid polarizer between the MPCA emitter and detector, and measuring the H and V channels as a function of the polarizer angle, θ . Figure 5(a) plots the normalized peak-to-peak THz voltage, for the H (blue) and V (red) channels, as a function of θ , where two strong lobes and two weaker lobes are evident for each channel. The weaker lobes can be better witnessed in Fig. 5(b), which presents a close-up of the center of Fig. 5(a).

This relatively complex angle-dependence can be understood with reference to Fig. 5(c), which illustrates the polarization state at each step in the experiment. There, the blue and red arrows represent the magnitude and direction of the H and V THz polarization states, which are horizontal and vertical when produced at the emitter (left-hand side of diagram). The axis of the wire-grid polarizer is shown by the gray arrow, while the axis of the detector (at 45°) is in green. Looking at the upper left of Fig. 5(c), when $\theta = 0^\circ$ the polarizer is parallel to H, and hence H passes through the polarizer, while V is blocked and is a minimum. The projection of H on the detector is shown in the upper center, while the detected signal is shown on the upper right. In this case, by looking at Fig. 5(a) at $\theta = 0^\circ$, the measured H signal is slightly over 0.8 but not at its maximum, which occurs at $\theta = 22.5^\circ$. In that case, the second row of Fig. 5(c) illustrates that part of H and V pass through the polarizer and are projected onto the detector, leading to the

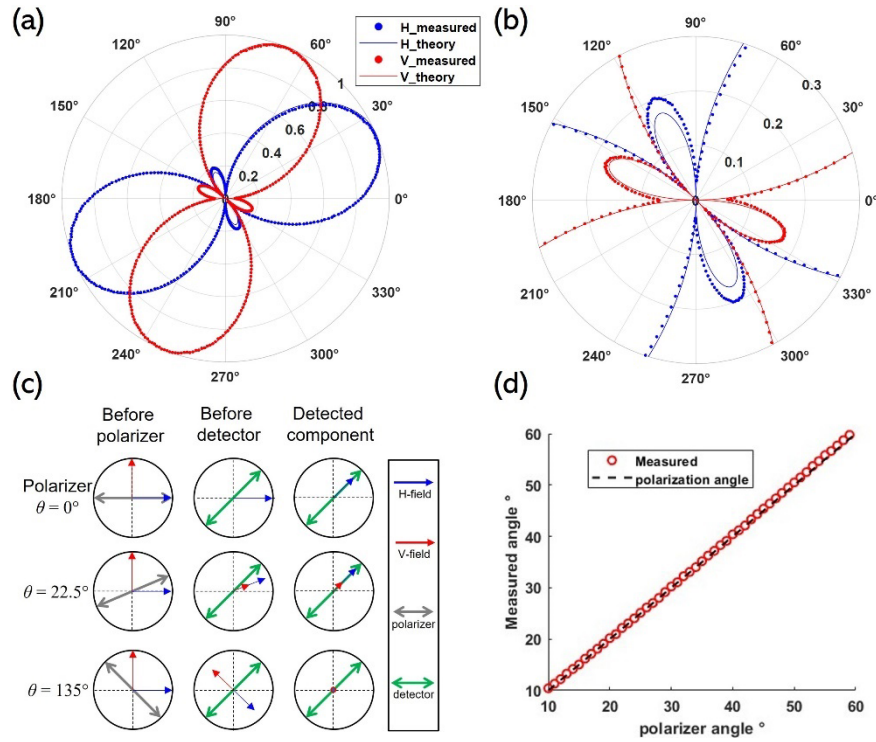


Fig. 5. Polarization responses of H and V as a function of the polarizer azimuthal angle, normalized from 0 to 1. (a) Measured peak-to-peak values of H and V by varying the polarizer angle from 0° to 360°. (b) Close-up center of (a). (c) Schematic of THz fields projected to the polarizer and the detector at three angles. (d) Relative changes of THz polarization angle measured by our PS THz-TDS for rotation of a wire-grid polarizer from 10° to 60° with a step of 1°.

largest detected H signal when the polarizer splits equally the angle formed between the H field and the detector. Similarly, by looking at the bottom row of Fig. 5(c), corresponding to $\theta = 135^\circ$, both H and V partially pass through the polarizer but are then polarized perpendicular to the detector, resulting in minimum signal detected in both channels (see Fig. 5(b) at $\theta = 135^\circ$).

The limited extinction ratio of the polarizer and the detector means that the minimum signal shown in Fig. 5(b) is not zero. With a known orientation angle of 45° of the detector, and the angle θ between the H field and the polarizer, the projection of the H field on the polarizer is $H \cos(\theta)$, and the subsequent projection on the detector is $H \cos(\theta) \cos(45 - \theta)$. Therefore, the measured signals of H and V can be expressed with the functions $f_H(\theta)$ and $f_V(\theta)$:

$$f_H(\theta) = |\cos(\theta) \cos(45^\circ - \theta)| \quad (1)$$

$$f_V(\theta) = |\cos(90 - \theta) \cos(45^\circ - \theta)| \quad (2)$$

where θ is the polarizer angle and $\theta = 0$ when the polarizer is horizontal (as shown in Fig. 6(c)). The calculated curves based on Eqs. (1) and (2) are presented as the solid black lines in Fig. 5(a) and (b). It is clear that $f_H(\theta)$ has maxima at $\theta = 22.5^\circ$ (and 202.5°) and minima at $\theta = 90^\circ$ (or 135° , 270° , 315°), which is in excellent agreement with the blue points shown in Fig. 5(a) and (b). This quantitative analysis agrees well with the above qualitative explanation discussed in Fig. 5(c). After passing through the wire-grid polarizer, the transmitted component of the

horizontal and vertical THz pulses are polarized at angle θ . To assess the polarization sensitivity of the system, we calculated the THz polarization angle by:

$$\theta_{meas} = \tan^{-1}\left(\frac{V}{H}\right)_{t'=0} \quad (3)$$

where $t' = 0$ corresponds to the peak of the demultiplexed signals H and V. The measured values of the polarization angle are shown as the points in Fig. 5(d), while the dashed line is a straight line. Close to 0° and 90° the measurement deviates from a straight line because of the finite extinction ratio of the wire-grid polarizer (Fig. S6 in Supplement 1). The standard deviation (rms deviation from the line) of the data in Fig. 5(d) is $\sigma_\theta = 0.16^\circ$, which represents the polarization accuracy of the system.

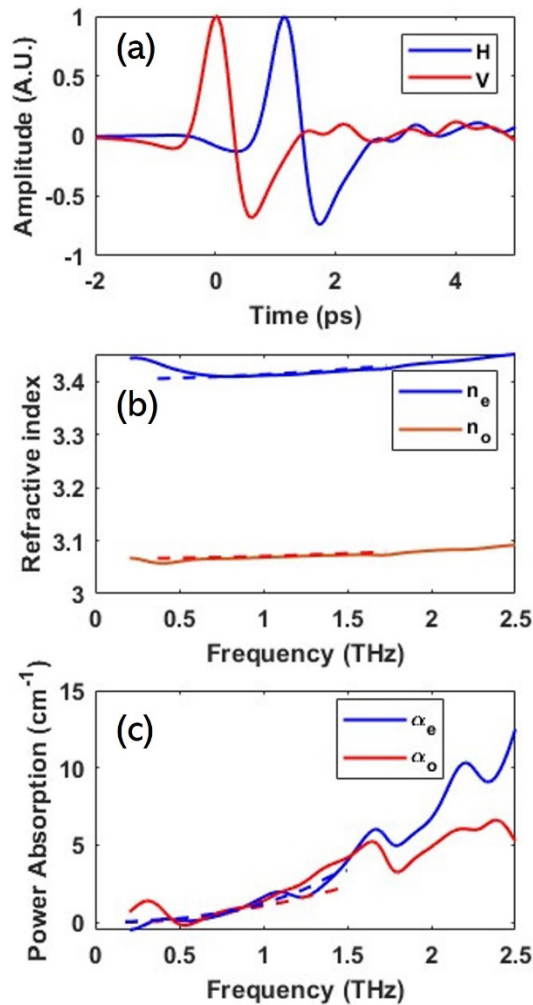


Fig. 6. PS THz-TDS measurement of crystalline sapphire in transmission. (a) Two pulses with a time delay after interacting with birefringent sapphire, normalized by the peak values. (b) Ordinary and extraordinary refractive index of sapphire. Dashed lines show the data of Ref. [33]. (c) Ordinary and extraordinary power absorption coefficient of sapphire.

3.3. Birefringence characterization

Birefringence effects in THz range have been explored for various materials. Crystals such as sapphire, ZnO and LiNbO₃ exhibit THz birefringence, as well as liquid crystals, metamaterials, polymers, textiles, wood and paper [32]. Studies of the THz birefringence are therefore important for materials characterization, and also to help to develop THz components (such as wave plates). In conventional THz-TDS, measurements of birefringent materials need to be conducted at least twice separately: first with the THz polarized along the ordinary principal axis, and then parallel to the extraordinary direction. In this work, we characterized the absorption and dispersion of crystalline sapphire in the frequency range of 0.2 to 2.5 THz, by simultaneously measuring both orthogonal THz fields. The sapphire was a 2-inch diameter, 1 mm thick disk with its c-axis in the plane of the disk. With the ordinary and extraordinary principal axes aligned to V and H, a THz transmission measurement was performed to extract its dielectric properties, as shown in Fig. 6.

Figure 6(a) shows two orthogonal pulses passing through the sapphire crystal. The different optical paths experienced by two fields were expressed as the time separation between two main pulses – V peaks at 0 ps and H peaks at 1.15 ps. If we ignore the dispersion effects on group velocity, the birefringence can be calculated by $\Delta n = \Delta t c / d = 0.34$, where Δt is the time separation between two channels, c is light speed in vacuum and d is the thickness of sapphire. To conduct a frequency analysis on absorption and dispersion of sapphire, we measured the other set of reference pulses without sample and performed Fourier analysis on two sets of pulses based on Fresnel equations and Beer-Lambert law. Figure 6(b) show the refractive index of ordinary and extraordinary axes. At 1 THz, the values of n_o and n_e are 3.07 and 3.41, and the birefringence is calculated as $\Delta n = n_e - n_o = 0.34$, corresponding to the value calculated by time separation of two pulses. Figure 6(c) shows the power absorption of ordinary and extraordinary axes. The power absorption increased at higher frequencies towards the phonon modes of sapphire. Given the measurement were performed in air, the absorption curves fluctuate at the water vapor absorption frequencies such as 1.67, 1.79 and 2.34 THz. The dashed lines in Fig. 6(b) and (c) indicate literature data [33]. Our results agree well with the literature values, and further extend the data of dielectric properties of sapphire to 2.5 THz. Note that if the optical axes of the sample are not known prior to measurement, they can be found by simply rotating the sample until the time delay between the H- and V-pulses is maximized, ensuring that the H and V pulses sample the major and minor axes of the refractive index ellipsoid.

3.4. Polarization sensitive imaging

THz imaging has proven to be valuable in diverse areas including, but not limited to, non-invasive inspection, material identification and tomographic reconstruction. Many studies have reported advanced THz imaging modalities, such as fast imaging, near-field imaging and passive imaging [2,34]. In most of the THz images presented, image contrast is generally explained as being caused by absorption or scattering. However, this explanation is sometimes ambiguous when it comes to anisotropic (birefringent) materials because the rotation of the THz polarization state will also reduce the amplitude measured by a polarization-sensitive THz detector, such as a photoconductive detector or electro-optic sampling. With additional access to the polarization angle, THz polarization imaging offers more information to interpret the object under imaging [14], and has been employed in tomographic measurements, stress analysis of fabric and paper, near-field THz imaging of bio matter [35] and investigations of the internal structure of polymeric materials [36–38].

Our measurement technique can also be readily applied to THz polarization imaging. To demonstrate the versatility of the system in polarization imaging, we studied a THz anisotropic metamaterial. Metamaterials are well known for their incredible capability to manipulate electromagnetic waves by simply engineering their unit cell. Here, we fabricated a gold metamaterial on a silicon substrate, with its contour forming a Chinese character of light (光), as

shown in Fig. 7(a). The unit cell of the metamaterial is shown in Fig. 7(b) which was an off-set H shaped meta-atom that essentially behaves as a resonant LC circuit [39,40]. Each meta-atom can be excited by the electric or magnetic fields of electromagnetic waves, which drive charges to accumulate at the extremities of the metal, and forming resonances at frequencies that scale directly with their dimensions [41]. In our structure, the asymmetric unit cell at sub-wavelength dimensions introduces anisotropy in the optical properties at THz frequencies.

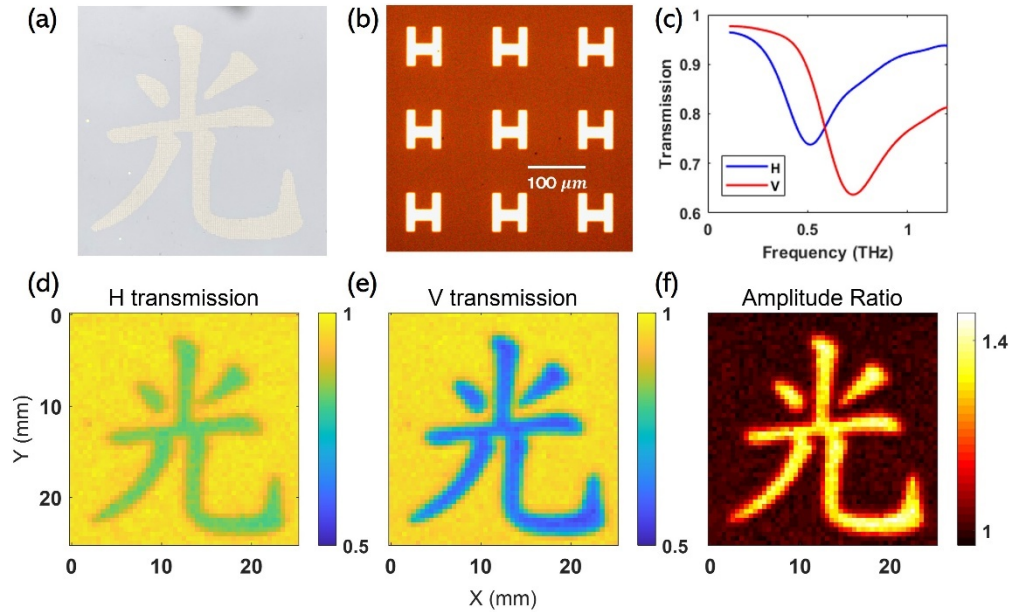


Fig. 7. Polarization sensitive imaging of metamaterial. (a) Optical image of metamaterial on silicon. The contour of metamaterial is designed to be the Chinese character for light (光). (b) Optical micrograph of individual meta-atoms, which are an offset H shape. (c) THz amplitude transmission of metamaterial for H (blue) and V (red) polarizations. (d-e) THz transmission images of the metamaterial at the resonance frequency for V polarization (0.72 THz), for (d) H-polarized and (e) V-polarized light. (f) Image of the detected amplitude ratio H to V at 0.72 THz.

Figure 7(c) shows the THz transmission spectra of the metamaterial obtained at a location within the 光 character. The H and V THz spectra (amplitude transmission relative to the substrate) have pronounced resonances from the metamaterial, with H resonant at 0.5 THz and V resonant at 0.72 THz. We obtained a THz image of the 光 character spatial profile of the metamaterial by raster scanning the sample and rapidly sampling the H and V THz waveform at each position. In Fig. 7(d-e) we present polarization- and frequency-resolved THz images of the 光 character as obtained from our PS-THz TDS at a spatial resolution of 0.5 mm. The normalized H and V transmission of the metamaterial at a frequency of 0.72 THz are shown in Fig. 7(d) and Fig. 7(e). At this frequency, the H and V transmission on bare silicon are the same, normalized to 1 (yellow areas). However, in the region of the 光 character, the H transmission is 80% while the V transmission is 56%, as a result of the anisotropic response of the metamaterial.

With access to the transmission images taken with the two polarization states, we can construct Fig. 7(f) by taking the detected amplitude ratio of H to V. The dark area of Fig. 7(f) is the clear bare substrate where H and V have the same transmission, so the amplitude ratio is almost equal to 1. The light area of Fig. 7(f) shows where H and V have different transmission as a result of the

metamaterial, and the amplitude ratio rises to about 1.4. The features of all the THz images have excellent agreement with the optical image shown in Fig. 7(a).

This approach more than halves the time required to obtain THz polarization images: polarization information is obtained at each pixel, rather than acquiring one polarization image, then changing the optical setup (e.g. rotating the sample or polarizer) and acquiring the other polarization. This also reduces any influence of systematic drift in the THz spectrometer's performance (e.g. laser power; humidity variations) by acquiring data simultaneously thereby reducing the measurement error further.

4. Conclusion

In this study, we report an innovative spectrometer capable of measuring full THz polarization states simultaneously, and without cross-talk. We fabricated a MPCA by using standard lithographic manufacturing, as a THz radiation source compatible with a compact 1550 nm femtosecond fibre laser. The performance of the emitter for each polarization channel was shown to be comparable to a commercial single-polarization antenna. We further proposed a multiplexing scheme to transfer two signals (horizontal and vertical THz polarization states) across one detector channel (photocurrent in a PCA detector) based on frequency modulation. We verified its versatility by analyzing THz spectra, characterizing birefringent sapphire, and imaging an anisotropic metamaterial structure.

By demonstrating the simultaneous measurement of orthogonal THz fields using a conventional H-dipole PCA detector we have provided a fast and precise measurement technique that is easily deployable for applications requiring polarization measurements, simply by replacing the THz source.

The system described herein measures one component of orthogonal THz fields. We note that it can be readily upgraded to perform generalized THz ellipsometry [42,43], where full elements of Jones matrix are measured instead of just measuring the diagonal elements as in conventional ellipsometry, by replacing the H-dipole detector with an interdigitated MPCA as detector. In this case, the horizontal and vertical electric field components will be directly obtained by the orthogonal electrodes of the detector, while H and V polarization states can be generated at the emitter and simultaneously detected via our multiplexing scheme.

Funding. National Science and Technology Council (NSTC 112-2222-E-110-002); Deutsche Forschungsgemeinschaft (Grant No. MA 1749/24-3); China Scholarship Council (CSC202106380055); Science and Technology Planning Project of Guangdong Province (2019B090909011); Guangdong Provincial Applied Science and Technology Research and Development Program (2019B090917007); National Natural Science Foundation of China (61988102); Engineering and Physical Sciences Research Council (EP/V047914/1).

Acknowledgements. Huiliang Ou would like to thank Dr Mark Crouch, Ms. Corinne Maltby and Mr. Frank Courtney for help fabricating and packing emitter and would like to thank Dr Xavier Romain's help on the metamaterial.

Disclosures. The authors declare no conflicts of interest.

Data availability. The data presented in this article are publicly available on Figshare at [44].

Supplemental document. See [Supplement 1](#) for supporting content.

References

1. D. Zimdars, J. S. White, G. Stuk, *et al.*, "Large area terahertz imaging and non-destructive evaluation applications," *Insight* **48**(9), 537–539 (2006).
2. R. I. Stantchev, X. Yu, T. Blu, *et al.*, "Real-time terahertz imaging with a single-pixel detector," *Nat. Commun.* **11**(1), 2535 (2020).
3. N. Karpowicz, H. Zhong, C. Zhang, *et al.*, "Compact continuous-wave subterahertz system for inspection applications," *Appl. Phys. Lett.* **86**(5), 054105 (2005).
4. B. E. Cole, J. B. Williams, B. T. King, *et al.*, "Coherent manipulation of semiconductor quantum bits with terahertz radiation," *Nature* **410**(6824), 60–63 (2001).
5. S. Whitmire, D. Wolpert, A. Markelz, *et al.*, "Protein flexibility and conformational state: A comparison of collective vibrational modes of wild-type and D96N bacteriorhodopsin," *Biophys. J.* **85**(2), 1269–1277 (2003).

6. C. Kulesa, "Terahertz spectroscopy for astronomy: From comets to cosmology," *IEEE Trans. Terahertz Sci. Technol.* **1**(1), 232–240 (2011).
7. T. Kleine-Ostmann and T. Nagatsuma, "A review on terahertz communications research," *J. Infrared, Millimeter, Terahertz Waves* **32**(2), 143–171 (2011).
8. A. Leitenstorfer, A. S. Moskalenko, T. Kampfrath, *et al.*, "The 2023 terahertz science and technology roadmap," *J. Phys. D: Appl. Phys.* **56**(22), 223001 (2023).
9. X. Chen, E. P. Parrott, Z. Huang, *et al.*, "Robust and accurate terahertz time-domain spectroscopic ellipsometry," *Photonics Res.* **6**(8), 768–775 (2018).
10. H. Fujiwara, *Spectroscopic ellipsometry: principles and applications* (John Wiley & Sons, 2007).
11. L. A. Nafie, T. Keiderling, and P. Stephens, "Vibrational circular dichroism," *J. Am. Chem. Soc.* **98**(10), 2715–2723 (1976).
12. X. Chen and E. Pickwell-MacPherson, "An introduction to terahertz time-domain spectroscopic ellipsometry," *APL Photonics* **7**(7), 071101 (2022).
13. D. M. Mittleman, J. Cunningham, M. C. Nuss, *et al.*, "Noncontact semiconductor wafer characterization with the terahertz Hall effect," *Appl. Phys. Lett.* **71**(1), 16–18 (1997).
14. N. C. Van der Valk, W. A. van der Marel, and P. C. Planken, "Terahertz polarization imaging," *Opt. Lett.* **30**(20), 2802–2804 (2005).
15. E. Castro-Camus, J. Lloyd-Hughes, M. Johnston, *et al.*, "Polarization-sensitive terahertz detection by multicontact photoconductive receivers," *Appl. Phys. Lett.* **86**(25), 254102 (2005).
16. H. Makabe, Y. Hirota, M. Tani, *et al.*, "Polarization state measurement of terahertz electromagnetic radiation by three-contact photoconductive antenna," *Opt. Express* **15**(18), 11650–11657 (2007).
17. A. Hussain and S. R. Andrews, "Ultrabroadband polarization analysis of terahertz pulses," *Opt. Express* **16**(10), 7251–7257 (2008).
18. N. Yasumatsu and S. Watanabe, "Precise real-time polarization measurement of terahertz electromagnetic waves by a spinning electro-optic sensor," *Rev. Sci. Instrum.* **83**(2), 023104 (2012).
19. N. Nemoto, T. Higuchi, N. Kanda, *et al.*, "Highly precise and accurate terahertz polarization measurements based on electro-optic sampling with polarization modulation of probe pulses," *Opt. Express* **22**(15), 17915–17929 (2014).
20. N. Yasumatsu, A. Kasatani, K. Oguchi, *et al.*, "High-speed terahertz time-domain polarimeter based on an electro-optic modulation technique," *Appl. Phys. Express* **7**(9), 092401 (2014).
21. K. Xu, E. Bayati, K. Oguchi, *et al.*, "Terahertz time-domain polarimetry (THz-TDP) based on the spinning E-O sampling technique: determination of precision and calibration," *Opt. Express* **28**(9), 13482–13496 (2020).
22. M. Nakagawa, M. Okano, and S. Watanabe, "Polarization-sensitive terahertz time-domain spectroscopy system without mechanical moving parts," *Opt. Express* **30**(16), 29421–29434 (2022).
23. K. Peng, D. Jevtics, F. Zhang, *et al.*, "Three-dimensional cross-nanowire networks recover full terahertz state," *Science* **368**(6490), 510–513 (2020).
24. A. Dreyhaupt, S. Winnerl, T. Dekorsy, *et al.*, "High-intensity terahertz radiation from a microstructured large-area photoconductor," *Appl. Phys. Lett.* **86**(12), 121114 (2005).
25. C. Mosley, M. Failla, D. Prabhakaran, *et al.*, "Terahertz spectroscopy of anisotropic materials using beams with rotatable polarization," *Sci. Rep.* **7**(1), 12337 (2017).
26. J. Van Rudd, J. L. Johnson, and D. M. Mittleman, "Cross-polarized angular emission patterns from lens-coupled terahertz antennas," *J. Opt. Soc. Am. B* **18**(10), 1524–1533 (2001).
27. J. V. Rudd, J. L. Johnson, and D. M. Mittleman, "Quadrupole radiation from terahertz dipole antennas," *Opt. Lett.* **25**(20), 1556–1558 (2000).
28. C. D. W. Mosley, M. Staniforth, A. I. H. Serrano, *et al.*, "Scalable interdigitated photoconductive emitters for the electrical modulation of terahertz beams with arbitrary linear polarization," *AIP Adv.* **9**(4), 045323 (2019).
29. C. D. W. Mosley, J. Deveikis, and J. Lloyd-Hughes, "Precise and accurate control of the ellipticity of THz radiation using a photoconductive pixel array," *Appl. Phys. Lett.* **119**(12), 121105 (2021).
30. R. Kohlhaas, S. Breuer, L. Liebermeister, *et al.*, "637 μ W emitted terahertz power from photoconductive antennas based on rhodium doped InGaAs," *Appl. Phys. Lett.* **117**(13), 131105 (2020).
31. J. Lloyd-Hughes, E. Castro-Camus, M. Fraser, *et al.*, "Carrier dynamics in ion-implanted GaAs studied by simulation and observation of terahertz emission," *Phys. Rev. B* **70**(23), 235330 (2004).
32. K. Wiesauer and C. Jördens, "Recent advances in birefringence studies at THz frequencies," *J. Infrared, Millimeter, Terahertz Waves* **34**(11), 663–681 (2013).
33. D. Grischkowsky, S. Keiding, M. Van Exter, *et al.*, "Far-infrared time-domain spectroscopy with terahertz beams of dielectrics and semiconductors," *J. Opt. Soc. Am. B* **7**(10), 2006–2015 (1990).
34. D. M. Mittleman, "Twenty years of terahertz imaging," *Opt. Express* **26**(8), 9417–9431 (2018).
35. R. I. Stantchev, J. C. Mansfield, R. S. Edginton, *et al.*, "Subwavelength hyperspectral THz studies of articular cartilage," *Sci. Rep.* **8**(1), 6924 (2018).
36. C. Jördens, M. Scheller, M. Wichmann, *et al.*, "Terahertz birefringence for orientation analysis," *Appl. Opt.* **48**(11), 2037–2044 (2009).
37. S. Katletz, M. Pflieger, H. Pühringer, *et al.*, "Polarization sensitive terahertz imaging: detection of birefringence and optical axis," *Opt. Express* **20**(21), 23025–23035 (2012).

38. M. Okano and S. Watanabe, "Anisotropic optical response of optically opaque elastomers with conductive fillers as revealed by terahertz polarization spectroscopy," *Sci. Rep.* **6**(1), 39079 (2016).
39. J. D. Baena, J. Bonache, F. Martin, *et al.*, "Equivalent-circuit models for split-ring resonators and complementary split-ring resonators coupled to planar transmission lines," *IEEE Trans. Microwave Theory Tech.* **53**(4), 1451–1461 (2005).
40. R. Marqués, F. Medina, and R. Rafii-El-Idrissi, "Role of bianisotropy in negative permeability and left-handed metamaterials," *Phys. Rev. B* **65**(14), 144440 (2002).
41. S. A. Ramakrishna, "Physics of negative refractive index materials," *Rep. Prog. Phys.* **68**(2), 449–521 (2005).
42. R. Azzam and N. Bashara, "Application of generalized ellipsometry to anisotropic crystals," *J. Opt. Soc. Am.* **64**(2), 128–133 (1974).
43. J. Hilfiker, B. Johs, C. Herzinger, *et al.*, "Generalized spectroscopic ellipsometry and Mueller-matrix study of twisted nematic and super twisted nematic liquid crystals," *Thin Solid Films* **455-456**, 596–600 (2004).
44. H. Ou, "Simultaneous measurement of orthogonal terahertz fields via an emission multiplexing scheme," *figshare*, (2023). <https://doi.org/10.6084/m9.figshare.24611124.v1>